Conformal quantum dot-SnO$_2$ layers as electron transporters for efficient perovskite solar cells

Minjin Kim[1][#], Jaeki Jeong[2][#], Haizhou Lu[2][#], Tae Kyung Lee[3], Felix T. Eickemeyer[2], Yuhang Liu[2], In-woo Choi[1], Seung Ju Choi[1], Yimhyun Jo[1], Hak-Beom Kim[1], Sung-In Mo[1], Young-Ki Kim[4], Heunjeong Lee[5], Na Gyeong An[6], Shinuk Cho[5], Wolfgang R. Tress[7], Shaik M. Zakeeruddin[2], Anders Hagfeldt[8], Jin Young Kim[6], Michael Grätzel[2*], Dong Suk Kim[1*]

[1]Ulsan Advanced Energy Technology R&D Center, Korea Institute of Energy Research, 25 Techno saneop-ro 55beon-gil, Nam-gu, Ulsan 44776, Republic of Korea.
[2]Laboratory of Photonics and Interfaces, Institute of Chemical Sciences and Engineering, École Polytechnique Fédérale de Lausanne (EPFL), CH-1015 Lausanne, Switzerland.
[3]Photovoltaics Research Department, Korea Institute of Energy Research (KIER), 152 Gajeong-ro, Yuseong-gu, Daejeon 34129, Republic of Korea.
[4]Central Research Facilities (UCRF), Ulsan National Institute of Science and Technology (UNIST), UNIST-Gil 50, Ulsan, 44919, Republic of Korea.
[5]Department of Physics and Energy Harvest Storage Research Center, University of Ulsan, Ulsan 44610, Republic of Korea.
[6]Department of Energy Engineering, School of Energy and Chemical Engineering, Ulsan National Institute of Science and Technology (UNIST), UNIST-Gil 50, Ulsan, 44919, Republic of Korea.
[7]Novel Semiconductor Devices Group, Institute of Computational Physics, Zurich University of Applied Sciences, Wildbachstr. 21, 8401 Winterthur, Switzerland.
[8]Department of Chemistry, Ångström Laboratory, Uppsala University, Box 523, 751 20 Uppsala, Sweden.

[#]These authors contributed equally to this work.
*Correspondence to: michael.graetzel@epfl.ch (M.G.), kimds@kier.re.kr (D.S.K.).

Abstract

Improvements to perovskite solar cells (PSCs) have focused on increasing their power conversion efficiency (PCE) and operational stability and maintaining high performance upon scale-up to module sizes. We report that replacing the commonly used mesoporous-titanium dioxide electron transport layer (ETL) with a thin layer of polyacrylic acid-stabilized tin(IV) oxide quantum dots (paa-QD-SnO$_2$) enhanced light capture and largely suppressed nonradiative recombination at the ETL-perovskite interface. The use of paa-QD-SnO$_2$ as electron-selective contact enabled PSCs (0.08 square centimeters) with a PCE of 25.7% (certified 25.4%) and high operational stability and facilitated the scale-up of the PSCs to larger areas. PCEs of 23.3, 21.7, and 20.6% were achieved for PSCs with active areas of 1, 20, and 64 square centimeters, respectively.

Main text

Efforts to realize metal halide perovskite solar cells (PSCs) with power-conversion efficiencies (PCEs) >23% have focused on formamidinium-rich lead iodide (FAPbI$_3$) formulations (*1-7*) because their narrower bandgap is closer to the Shockey-Queisser optimum than for methylammonium-based or mixed-halide perovskites (*8*). By fully using the broad absorption spectrum of FAPbI$_3$, a certified PCE of 25.21% with a short-circuit current density (J_{sc}) of >26

mA/cm^2 was obtained for the mesoporous-structure PSCs (*7*). However, the mesoporous-TiO$_2$ (m-TiO$_2$) electron-transport layer (ETL) may show unwanted photocatalytic effects under ultraviolet (UV) light illumination and the low electron mobility of m-TiO$_2$ limits the charge transport (*9-11*).

Among alternative metal oxide ETLs (*10-17*) for PSCs, SnO$_2$-based PSCs could potentially be more efficient and stable given that SnO$_2$ is UV resistant, has a higher carrier mobility than TiO$_2$ that facilitates electron extraction and transport (*10-12*). Several techniques, such as spin coating (*11, 16*), atomic layer deposition (*1*) and chemical bath deposition (CBD) (*12, 17*), have been used to deposit the SnO$_2$ ETLs. Spin-coated SnO$_2$ ETL from a SnO$_2$ colloidal quantum dots (QD-SnO$_2$) solution onto the indium doped tin oxide (ITO) substrate enabled a certified PCE of >23% for the corresponding planar-structure PSCs (*2, 16*). Recently, a thin SnO$_2$ ETL on fluorine-doped tin oxide (FTO) deposited with a well-controlled CBD method enabled PSCs with a certified PCE of 25.19% because of the improved carrier properties of SnO$_2$ ETL (*17*). However, compared with the m-TiO$_2$-based PSCs, the SnO$_2$-based PSCs still suffered from a relatively low J_{sc} of <26 mA/cm^2, that is attributed to the optical losses arising from reflection and destructive interference of the incident light waves at the interfaces.

One approach to reduce these optical losses is to use the textured surface of FTO as the front contact which scatters the incoming radiation, destroying the coherence of the incoming light and affording light trapping by increasing the optical path length (*18*). The enhanced light absorption by the perovskite benefits the photocurrent delivered by the photovoltaic (PV) cell. Similar strategies have been used for textured crystalline-silicon based PSCs (*19*). However, early efforts to deposit a thin, uniform and high-quality SnO$_2$ ETL using a solution process were incompatible with the underlying textured FTO surface (*1, 12, 20-22*), causing optical losses. The highest reported J_{sc} of SnO$_2$-based PSCs of ~25.2 mA/cm^2 (*17, 20*) still limits the overall PV performance.

Here we introduce a new architecture for the ETL of PSCs that consists of a compact-TiO$_2$ (c-TiO$_2$) blocking layer covered by a thin layer of polyacrylic-acid (PAA)-stabilized-QD-SnO$_2$ (paa-QD-SnO$_2$) deposited in a contiguous and conformal manner on the textured FTO. The uniform bilayer of paa-QD-SnO$_2$@c-TiO$_2$ largely improved the perovskite's absorption of sun light and formed an outstanding electron-selective contact with the perovskite film. The quantum size effect increased the band gap of the QD-SnO$_2$ from 3.6 eV for bulk SnO$_2$ to ~4 eV (*21, 23*) and produced a corresponding upward shift of its conduction band edge energy. This shift aligned it well with the conduction band edge of the perovskite so that electron capture by the SnO$_2$-based ETL proceeded with minimal energy losses (*5, 11, 16, 21*).

PAA, a polymer binder, was added to the SnO$_2$ QDs solution to attach the colloidal QD-SnO$_2$ firmly to the c-TiO$_2$ surface providing a contiguous, thin, and conformal SnO$_2$ layer that fully covered the c-TiO$_2$ layer underneath. Importantly, the carboxyl groups of PAA undergo strong hydrogen and coordinative bonding with the metal oxide surface, facilitating the lamination process, especially for production on a large scale (*24-26*). By choosing FTO substrates with suitable diffuse transmittance and reflectance, the textured paa-QD-SnO$_2$@c-TiO$_2$ bilayer enabled a PCE of 25.7% (certified 25.4%) with a J_{sc} of 26.4 mA/cm^2 and high stability for the corresponding PSCs. We further demonstrate that the paa-QD-SnO$_2$@c-TiO$_2$ bilayer could be applied to realize large PSC modules with an active area up to 64 cm^2 maintaining a PCE of >20%.

99 We investigated the microstructures of the spin-coated QD-SnO$_2$ layer on the c-TiO$_2$ using
100 commercially available SnO$_2$ colloidal QDs with and without PAA. Unless otherwise
101 mentioned, the QD-SnO$_2$ solution was diluted by deionized water (1:20) in this study. Fig. S1,
102 a-c, show the top-view scanning electron microscope (SEM) images of the c-TiO$_2$, QD-
103 SnO$_2$@c-TiO$_2$ and paa-QD-SnO$_2$@c-TiO$_2$, respectively. Because of the textured surface, the
104 c-TiO$_2$ layer was not fully covered by the spin-coated QD-SnO$_2$ (Fig. S1b). In contrast, a
105 uniform, conformal paa-QD-SnO$_2$ layer was formed (Fig. S1c). Atomic force microscopy
106 (AFM) images (Fig. S1, d-f) further confirmed the uniform morphology of the paa-QD-
107 SnO$_2$@c-TiO$_2$ (Fig. S1f), which is different from that of the QD-SnO$_2$@c-TiO$_2$ (Fig. S1e).
108
109 Fig. 1, A and B, show the cross-sectional transmission electron microscopy (TEM) images of
110 the QD-SnO$_2$@c-TiO$_2$ and paa-QD-SnO$_2$@c-TiO$_2$ bilayers on FTO substrates, respectively.
111 The QD-SnO$_2$@c-TiO$_2$ bilayer presented an ununiform distribution over the FTO surface with
112 a thickness varied from ~30 (vertex region) to ~70 nm (valley region), while the paa-QD-
113 SnO$_2$@c-TiO$_2$ bilayer had a uniform and conformal distribution over the FTO surface with a
114 uniform thickness of ~30 nm. The different distribution between QD-SnO$_2$ and paa-QD-SnO$_2$
115 layers can also be seen clearly from the cross-sectional SEM images (Fig. S2, a and b),
116 suggesting that PAA played a key role in forming the uniform and contiguous layer of paa-
117 QD-SnO$_2$ ETL as shown in Fig. S3.
118
119 Element mapping with energy-disperse x-ray spectroscopy (EDS) of Ti (Fig. 1, C and D) and
120 Sn (Fig. 1, E and F) revealed a coverage of TiO$_2$ and SnO$_2$ over the FTO surface for both QD-
121 SnO$_2$@c-TiO$_2$ and paa-QD-SnO$_2$@c-TiO$_2$ bilayers. The selected area electron diffraction
122 (SAD) generated by TEM for the paa-QD-SnO$_2$@c-TiO$_2$ bilayer (Fig. S4) showed that both
123 QD-SnO$_2$ and c-TiO$_2$ were polycrystalline. The paa-QD-SnO$_2$ had a particle size of ~4 nm (Fig.
124 S4c), which is also confirmed by the TEM images (Fig. S5, a-c) and dynamic light scattering
125 analysis (Fig. S5, d and e).
126
127 The interactions between PAA and QD-SnO$_2$ were studied by the x-ray photoelectron
128 spectroscopy (XPS) (Fig. S6) and fourier transform infrared spectroscopy (FTIR)
129 measurements (Fig. S7). It is clear from the XPS measurements that both QD-SnO$_2$@c-TiO$_2$
130 and paa-QD-SnO$_2$@c-TiO$_2$ bilayers showed characteristic peaks attributed to Sn (Fig. S6a);
131 however, the Sn $3d$ peaks of paa-QD-SnO$_2$ shifted to high binding energy by ~0.2 eV compared
132 with that of QD-SnO$_2$, indicating that PAA was bonded to the QD-SnO$_2$. No obvious difference
133 was observed for the O $1s$ characteristic peaks (Fig. S6, b-d). FTIR measurements showed
134 peaks at ~2954 and ~1716 cm^{-1} that arise from C–H and C=O stretching vibrations of PAA
135 (Fig. S7a) and a characteristic peak at ~574 cm^{-1} of the Sn-O vibration (Fig. S7b). The Sn-O
136 peak shifted to ~594 cm^{-1} for the paa-QD-SnO$_2$, and the C–H and C=O stretching vibrations
137 shifted to ~3012 and ~1628 cm^{-1}, respectively (Fig. S7c), demonstrating that PAA interacted
138 with QD-SnO$_2$ (*27*).
139
140 We chose FAPbI$_3$ as the perovskite layer and details of its fabrication can be found in the
141 supplementary materials (SM) or the previous report (*3*). Top-view SEM images of the FAPbI$_3$
142 films spin-coated on different ETLs, including c-TiO$_2$, m-TiO$_2$@c-TiO$_2$, QD-SnO$_2$@c-TiO$_2$
143 and paa-QD-SnO$_2$@c-TiO$_2$ are shown in Fig. S8, a to d, respectively. Compact and dense
144 surface morphologies were observed for all the perovskite films. Figure S9a showed identical
145 x-ray diffraction (XRD) peak positions for all samples at 14.1° and 28.2°, which correspond to
146 the (001) and (002) crystal planes of α-FAPbI$_3$ (*3-5*). All the perovskite films had identical full-
147 width at half-maximum (FWHM) for the main (001) peak (Fig. S9b). We conclude that the

morphology and crystallinity of the perovskite films are not affected significantly by the different ETLs.

The PSCs with an active area of 0.08 cm^2 were fabricated in a conventional n-i-p structure (FTO/ETL/perovskite/OAI/spiro-MeOTAD/Au), where OAI is octylammonium iodide, spiro-MeOTAD is 2,2',7,7'-tetrakis[N,N-di(4-methoxyphenyl)amino]-9,9'-spirobifluorene. We performed the quasi-steady-state current-voltage (QSS-IV) measurement (Fig. 2A), which was employed for the certification of PSCs by the National Renewable Energy Laboratory (NREL) and Newport Inc. Details of the QSS-IV measurements are given in the SM. All the PSCs were fully aged in the ambient condition for 100 hours before the measurements.

The c-TiO$_2$-based cell had a low PCE of 17.27% under the QSS-IV measurement. For the m-TiO$_2$@c-TiO$_2$ based PSC, a PCE of 23.74% with a short-circuit current density (J_{sc}) of 25.74 mA/cm^2, an open-circuit voltage (V_{oc}) of 1.142 V and a fill-factor (FF) of 80.79% was obtained, which is consistent with the previous reports (3, 7). Compared with the mesoporous-structured devices, the QD-SnO$_2$@c-TiO$_2$ based cell had a higher V_{oc} of 1.164 V, but a lower J_{sc} of 25.12 mA/cm^2, resulting a PCE of 23.29%. The J_{sc} of the QD-SnO$_2$@c-TiO$_2$-based PSC is similar to the values reported for the SnO$_2$-based cells in the literature (17, 20). With the paa-QD-SnO$_2$@c-TiO$_2$ ETL, the PSC exhibited a high PCE of 25.18% with a considerably improved J_{sc} of 26.28 mA/cm^2, V_{oc} of 1.177 V and FF of 81.49%, matching the 25.39% efficiency certified by Newport Inc (Figs, S10 and S11).

The conventional J-V measurements under both forward and reverse scans were also performed (Fig. S12). The detailed PV parameters are summarized in table S1. There is a significantly different PV value obtained for the c-TiO$_2$-based cell under QSS-IV (Fig. 2A) and conventional J-V measurements (Fig. S12a), while the other cells showed similar PV results, indicating that c-TiO$_2$-based cell is unstable and the single c-TiO$_2$ layer is not a proper ETL for PSCs (28, 29). The contrasting feature of the c-TiO$_2$-based cell compared to the other cells in Fig. 2A and Fig. S12a is discussed in note S1. Hereafter, the c-TiO$_2$-based cells will not be discussed. A statistic distribution of the PCE of all the PSCs (Fig. 2B) showed that the paa-QD-SnO$_2$@c-TiO$_2$-based PSC had the highest averaged values. Details of the statistic PV parameters of all different ETL-based cells are shown in Fig. S13. Hereafter, we chose the paa-QD-SnO$_2$@c-TiO$_2$-based cell as the target in the following discussions.

The J_{sc} of the PSCs measured under the solar simulator was verified with external quantum efficiency (EQE) measurements. The target cell had slightly higher EQE than the m-TiO$_2$@c-TiO$_2$-based PSC over the entire absorption spectrum (Fig. 2C), resulting in a higher integrated J_{sc} of 26.01 mA/cm^2; however, a relatively lower integrated J_{sc} of 25.06 mA/cm^2 was obtained for the QD-SnO$_2$@c-TiO$_2$-based device than that (25.69 mA/cm^2) of m-TiO$_2$@c-TiO$_2$-based cell. The high J_{sc} of the target cell was attributed to the desired light scattering that prolongs the optical length, enhancing the light absorption by the perovskite with the conformal structured paa-QD-SnO$_2$@c-TiO$_2$ bilayer over the FTO substrate. This is confirmed with highest diffuse transmittance (haze) of paa-QD-SnO$_2$@c-TiO$_2$ when compared to the other ETLs shown in Fig. S14a. The higher transmittance of paa-QD-SnO$_2$@c-TiO$_2$ than the QD-SnO$_2$@c-TiO$_2$ (Fig. S14b) may be traced back to the thinner film thickness as shown in the optical simulations (Fig. S14, c and d), which could also contribute to the high J_{sc}. We further compared the J_{sc} obtained for the paa-QD-SnO$_2$@c-TiO$_2$-based PSCs using different substrates (Fig. S15). The Asahi FTO glass with high diffuse transmittance was the most suitable substrate for achieving a high J_{sc}.

4

198 The effect of the ETL composition on the photon flux emitted by the PSCs measured in steady-
199 state at an excitation photon flux equivalent to 1 sun is shown in Fig. 2D. The investigated
200 devices were complete solar cells without the Au back contact. Compared to the m-TiO$_2$@c-
201 TiO$_2$ and QD-SnO$_2$@c-TiO$_2$ based devices, the target cell had significantly higher
202 photoluminescence (PL) intensity, reaching a PL quantum yield (PLQY) of 7.5%. This
203 indicates a reduced non-radiative recombination at the interface between perovskite and paa-
204 QD-SnO$_2$ ETL. Details of the measurements and calculations of PLQY are shown in note S2.
205 From the PLQY measurements, we derived the quasi-Fermi level splitting (ΔE_F) in the
206 perovskite under 1 sun illumination (note S3) and compared the (ΔE_F) with the V_{oc} measured
207 from the same device. ΔE_F and V_{oc} showed the same trend indicating that the V_{oc} increase can
208 be partly attributed to the reduced non-radiative recombination. The $\Delta E_F/q$-V_{oc} offset (where q
209 is the elementary charge), however, is different. For the target cell it is 10 mV lower than that
210 of the m-TiO$_2$@c-TiO$_2$ based cells, indicating a better energetic alignment at the interfaces (30).

212 Ultraviolet photoelectron spectroscopy (UPS) measurements on the surface of different ETLs
213 (Fig. S16) showed that the conduction band of paa-QD-SnO$_2$ matched better with perovskite
214 than the m-TiO$_2$@c-TiO$_2$, which could facilitate the charge transfer from perovskite to the ETL
215 (Fig. S17). Detailed analysis of the UPS data is shown in note S4. Fig. S18, a and b, show the
216 time-resolved PL (TRPL) spectra of the perovskite films on different ETLs measured from
217 both the perovskite and the glass sides. The perovskite film deposited on paa-QD-SnO$_2$@c-
218 TiO$_2$ had the fastest decay among all the samples. Since it has low non-radiative recombination
219 rate, the fast decay is dominated by the favored interfacial electron transfer. The electron
220 mobility measurements (Fig. S18c) revealed that the paa-QD-SnO$_2$@c-TiO$_2$ layer had the
221 highest carrier mobility. All these results indicate a superior charge extraction from perovskite
222 to the paa-QD-SnO$_2$ ETL.

224 Regarding the reduced non-radiative recombination, we determined the EQE of
225 electroluminescence (EQE$_{EL}$) on representative PSC devices. Fig. 2E shows an EQE$_{EL}$ of 12.5%
226 for the target cell at an injection current density of 26 mA/cm^2 corresponding to the J_{sc} under
227 1 sun illumination, whereas the m-TiO$_2$@c-TiO$_2$ and QD-SnO$_2$@c-TiO$_2$ based cells have an
228 EQE$_{EL}$ of 2.5% and 8.3%, respectively, under the same conditions. Thus, the non-radiative
229 recombination rate in the PSC was reduced over 5 times simply by replacing the m-TiO$_2$ with
230 a paa-QD-SnO$_2$ electron-selective contact layer. The obtained highest V_{oc} of 1.22 V (Fig. S19),
231 [which is near the V_{oc} predicted from EQE$_{EL}$ according to the reciprocity theorem (31, 32)]
232 measured without the metal mask reached 98% of the radiative limit V_{oc} (1.25 V) (2, 5). We
233 also conducted transient photovoltage measurements for the PSCs (Fig. S20a). The target cell
234 showed a slower V_{oc} decay than the reference cells, indicating a slower charge recombination
235 rate. The dark J-V curves (Fig. S20b) showed the lowest reverse saturation current for the target
236 cell, pushing the on-set of the dark current to highest voltages, which also reflected the lowest
237 interfacial non-radiative recombination.

239 Fig. 2F shows the light-intensity dependent V_{oc} measurements for the PSCs. For both the
240 reference and target cells, the measured V_{oc} was linearly dependent on the logarithm of the light
241 intensity. The diode ideality factor n_{id}, deduced from the slope described by $n_{id}k_BT/q$, where
242 k_B is the Boltzmann constant and T is temperature, was 1.83, 1.79 and 1.46 for the the m-
243 TiO$_2$@c-TiO$_2$, QD-SnO$_2$@c-TiO$_2$ based cells and the target cell, respectively. The reduced n_{id}
244 contributed to the increased FF of the target cell as the FF critically depends on the n_{id} (33).
245 The reduced n_{id} is also consistent with the PLQY, TRPL, EQE$_{EL}$, transient photovoltage decay
246 and dark J-V measurements, unambiguously supporting the conclusion of reduced non-
247 radiative recombination of the target PSC using paa-QD-SnO$_2$ ETL. This manifests itself by

5

248   much stronger photo- and electroluminescence (Fig 2, C and D) as well as a lower ideality
249   factor (Fig. 2E) enabling very high fill factor of 83.8 % to be reached by our target device (table
250   S2). Further strong support for our conclusion comes from the observation of a slower transient
251   photovoltage decay (Fig. S20a) and higher electron mobility (Fig. S20b) as well as the dark J-
252   V measurements of the paa-QD-SnO$_2$@c-TiO$_2$ based cell compared to the control devices. The
253   significant reduction of the trap-assisted non-radiative recombination is the main reason for the
254   reduced V_{oc} deficit of our target cell of ~310 mV as compared to ~350 mV for the mesoporous-
255   structure cell [bandgap of our perovskite film was calculated to be 1.53 eV (*3*)], which is one
256   of the lowest values reported in the field of PSCs.

258   Scaling up of the PSCs to module size is another requirement for their commercial exploitation.
259   We used paa-QD-SnO$_2$@TiO$_2$ ETL to fabricate perovskite solar mini-modules with active
260   areas up to 64 cm^2. Details of the fabrication process for the solar modules can be found in the
261   SM and movie S1. Fig. 3A shows the J-V curves and images of the perovskite mini modules
262   with different active areas. The highest PCEs achieved for the PSCs with active areas of 1, 20
263   and 64 cm^2 were 23.3%, 21.7% and 20.6%, respectively. Movie S2 shows a typical
264   measurement for the 64 cm^2 perovskite solar modules. Fig. S21a illustrates a solar module with
265   sub-cells connected in series with a magnified view of the contact connections and a
266   geometrical FF (GFF) was calculated to be 95.6% according to the SEM images (Fig. S21b) of
267   the interconnections. Details of the PV parameters are summarized in table S2. The decrease
268   of the PCE with increased device size is mainly caused by a decreased FF. The V_{oc} of the
269   module (table S2) divided by the number of stripes is 18.5 volt /16 = 1.156 V, which is equal
270   to the V_{oc} of the 1 cm^2 cell. Hence, there is no additional V_{oc} loss in the module. Therefore, we
271   attribute the FF decrease to the increased series resistance, including transport layer resistances,
272   contact resistances and interconnect resistance. We sent the PSC modules to an independent
273   laboratory (OMA company, Republic of Korea) for certification. PCEs of 21.66% (Fig. S22)
274   and 20.55% (Fig. S23) were confirmed for the PSC mini modules with active areas of 20 and
275   64 cm^2, respectively, which agreed well with the measurements in our laboratory, and are
276   compared with other reported values in Fig. S24.

278   We further compared the statistical distribution of the PCEs for the mesoporous-based (Fig.
279   3B) and target (Fig. 3C) perovskite mini modules. For the perovskite modules with the same
280   active area (1, 20 or 64 cm^2), the target modules had higher averaged PCE and narrower PCE
281   distributions than the mesoporous-based modules. The averaged PCE of the 64 cm^2 PSC
282   module increased by ~30% by simply replacing the m-TiO$_2$ with paa-QD-SnO$_2$, indicating that
283   the paa-QD-SnO$_2$ could be uniformly coated on the large size substrates. The statistical
284   distribution of the PV parameters (Fig. S25) further revealed that the V_{oc} and FF of the
285   mesoporous-based modules decreased significantly more than that of the target PSC modules.
286   The shunt resistance of our solar modules retained a typical value of >4000 $\Omega \cdot cm^2$ (table S3),
287   indicating that losses from leakage currents across shunts produced during scale up are
288   negligible. We attribute the small decrease of V_{oc} and FF for the target PSC modules to the low
289   contact resistance (Fig. S26, a and b) because of the easier laser scribing as well as low series
290   resistance and low interfacial defects of paa-QD-SnO$_2$@c-TiO$_2$ bilayer.

292   Fig. 4A shows the 1000-hour shelf life tested with unsealed devices in ambient air at 25%
293   relative humidity (RH) and 25 °C. The target PSC retained 80% of the maximum PCE (25.7%)
294   after 1000-hour storage, whereas the m-TiO$_2$@c-TiO$_2$ and QD-SnO$_2$@c-TiO$_2$ based PSCs
295   decreased almost 30% and 40% of the initial efficiency, respectively, indicating that the target
296   cell is more resistant to the moisture and oxygen than the widely used mesoporous structured
297   PSCs. We also performed the operational stability test for the unsealed devices in a N$_2$

6

environment under MPP tracking conditions using a LED lamp with a calibrated light intensity of 100 mW/cm^2. More details about the MPP tests can be found in the SM and in the previous reports (5, 7). Fig. 4B shows that the target cell had higher PCE than the reference cell during the 350-hour MPP tracking test. From the detailed PV parameters during the MPP tracking measurements (Fig. S27), it's clear that the higher performance of the target PSC is because of the higher and rather stable V_{oc}, which decreased less compared with the reference cells. The main degradation of the target cell is the decline of FF (Fig. S27), which is attributed to the de-doping of lithium from the hole-transport layer (HTL) (5, 34).

We further tested the sealed devices under ambient conditions. Fig. S28 showed that 70.5% of the initial efficiency of the target cell retained after 700-hour light-soaking test, whereas the m-TiO$_2$@c-TiO$_2$ based cell declined 45% over the same testing time. To assess the suitability of the cells for real applications, we performed MPP stability test for the encapsulated target cell under ambient conditions. Fig. S29 showed that 95% of the initial efficiency retained for the sealed target cell after 100 hours MPP tracking and 2 hours dark recovery under ambient conditions. The substantial decline of FF is still the main reason for the performance loss. Future studies of additive-free HTLs will be conducted to enhance the stability of PSCs.

References:

(1) S. Turren-Cruz, et al. Methylammonium-free, high-performance, and stable perovskite solar cells on a planar architecture. *Science* **362**, 449-453 (2018).

(2) Q. Jiang, et al. Surface passivation of perovskite film for efficient solar cells. *Nat. Photonics* **13**, 460-466 (2019).

(3) M. Kim, et al. Methylammonium chloride induces intermediate phase stabilization for efficient perovskite solar cells. *Joule* **3**, 2179-2192 (2019).

(4) H. Min, et al. Efficient, stable solar cells by using inherent bandgap of α-phase formamidinium lead iodide. *Science* **366**, 749-753 (2019).

(5) H. Lu, et al. Vapor-assisted deposition of highly efficient, stable black-phase FAPbI$_3$ perovskite solar cells. *Science* **370**, eabb8985 (2020).

(6) H. Lu, et al. Compositional and Interface Engineering of Organic-Inorganic Lead Halide Perovskite Solar Cells. *iScience*, **23**, 101359 (2020).

(7) J. Jeong, et al. Pseudo-halide anion engineering for α-FAPbI$_3$ perovskite solar cells. *Nature* **592**, 381-385 (2021).

(8) G. E. Eperon, et al. Formamidinium lead trihalide: a broadly tunable perovskite for efficient planar heterojunction solar cells. *Energy Environ. Sci.* **7**, 982-988 (2014).

(9) T. Leijtens, et al. Overcoming ultraviolet light instability of sensitized TiO$_2$ with meso-superstructured orgamometal tri-halide perovskite solar cells. *Nat. Commun.* **4**, 2885 (2013).

(10) Q. Jiang, et al. SnO$_2$: A wonderful electron transport layer for perovskite solar cells. *Small* **14**, 1801154 (2018).

(11) Q. Jiang, et al. Enhanced electron extraction using SnO$_2$ for high-efficiency planar-structure HC(NH$_2$)PbI$_3$-based perovskite solar cells. *Nature Energy* **2**, 16177 (2017).

(12) E.H. Anaraki, et al. Highly efficient and stable planar perovskite solar cells by solution-processed tin oxide. *Energy Environ. Sci.* **9**, 3128-3134 (2016).

(13) R. Chen, et al. High-efficiency, hysteresis-less, UV-stable perovskite solar cells with cascade ZnO-ZnS electron transport layer. *J. Am. Chem. Soc.* **141**, 541-547 (2019).

(14) S.S. Shin, et al. High-performance flexible perovskite solar cells exploiting Zn$_2$SnO$_4$ prepared in solution below 100 ℃. *Nat. Commun.* **6**, 7410 (2015).

(15) S.S. Shin, et al. Colloidally prepared La-doped BaSnO$_3$ electrodes for efficient, photostable perovskite solar cells. *Science* **356**, 167-171 (2017).

348 (16) G. Yang, et al. Stable and low-photovoltage-loss perovskite solar cells by multifunctional
349 passivation, *Nat. Photon.* **15**, 681-689 (2021).
350 (17) J.J. Yoo, et al. Efficient perovskite solar cells via improved carrier management. *Nature*
351 **590**, 587-593 (2021).
352 (18) S. Manzoor, et al. Improved light incoupling in planar solar cells via improved texture
353 morphology of PDMS scattering layer. *IEEE 44th Photovoltaic Specialist Conference,* 1228-
354 1232 (2017).
355 (19) Y. Hou, et al. Efficient tandem solar cells with solution-processed perovskite on textured
356 crystalline silicon. *Science* **367**, 1135-1140 (2020).
357 (20) Y. Zhang, et al. Achieving reproducible and high-efficiency (>21%) perovskite solar cells
358 with a presynthesized $FAPbI_3$ powder. *ACS Energy Lett*. **5**, 360-366 (2020).
359 (21) M.M. Tavakoli, et al. Mesoscopic oxide double layer as electron specific contact for highly
360 efficient and UV stable perovskite photovoltaics. *Nano Lett*. **18**, 2428-2434 (2018).
361 (22) T. Bu, et al. Universal passivation strategy to slot-die printed SnO_2 for hysteresis-free
362 efficient flexible perovskite solar module. *Nat. Commun*. **9**, 4609 (2018).
363 (23) A. Das, et al. The role of SnO_2 quantum dots in improved CH_4 sensing at low temperature.
364 *J. Mater. Chem. C* **2**, 164-171 (2014).
365 (24) B. Hu, et al. Understanding of pre-lithiation of poly(acrylic acid) binder: Striking the
366 balances between the cycling performance and slurry stability for silicon-graphite composite
367 electrodes in Li-ion batteries. *J. Power Sources* **416**, 125-131 (2019).
368 (25) L. Wei, et al. High performance polymer binders inspired by chemical shifting of textiles
369 for silicon anodes in lithium ion batteries. *J. Mater. Chem. A*. **5**, 22156-22162 (2017).
370 (26) P. Parikh, et al. Role of polyacrylic acid (PAA) binder on the solid electrode interphase in
371 silicon anodes. *Chem. Mater*. **31**, 2535-2544 (2019).
372 (27) D. Yang, et al. High efficiency planar-type perovskite solar cells with negligible hysteresis
373 using EDTA-complexed SnO_2. *Nat. Commun.* **9**, 3239 (2018).
374 (28) J. Ji, et al. Two-stage ultraviolet degradation of perovskite solar cells induced by the
375 oxygen vacany-Ti^{4+} states. *iScience* **23**, 101013 (2020).
376 (29) M. M. Tavakoli, et al. Surface engineering of TiO_2 ETL for highly efficient and hysteresis-
377 less planar perovskite solar cells (21.4%) with enhanced open-circuit voltage and stability. *Adv.*
378 *Energy Mater*. **8**, 1800794 (2018).
379 (30) P. Caprioglio, et al. On the relation between the open-circuit voltage and quasi-Fermi level
380 splitting in efficient perovskite solar cells. *Adv. Energy Mater*. **9**, 1901631 (2019).
381 (31) U. Rau, Reciprocity relation between photovoltaic quantum efficiency and
382 electroluminescent emission of solar cells. *Phys. Rev. B* **76**, 085303 (2007).
383 (32) W. Tress, et al. Predicting the open-circuit voltage of $CH_3NH_3PbI_3$ perovskite solar cells
384 using electroluminescence and photovoltaic quantum efficiency spectra: the role of radiative
385 and non-radiative recombination. *Adv. Energy Mater*. **5**, 1400812 (2015).
386 (33) M. Green, et al. Accuracy of analytical expressions for solar cell fill factors. *Solar Cells*
387 **7**, 337-340 (1982).
388 (34) Y. Wang, et al. Stabilizing heterostructures of soft perovskite semiconductors. *Science*
389 **365**, 687-691 (2019).
390 (35) N.J. Jeon, et al. Compositional engineering of perovskite materials for high-performance
391 solar cells. *Nature* **517**, 476-480 (2015).
392 (36) M. Kim, et al. Effects of cation size and concentration of cationic chlorides on the properties of
393 formamidinium lead iodide based perovskite solar cells. *Sustainable Energy Fuels* **4**, 3753-3763
394 (2020).
395 (37) R. T. Ross, et al. Some thermodynamics of photochemical systems. *J. Chem. Phys.* **46**,
396 4590-4593 (1967).

397 (38) P. Wurfel, et al. The chemical potential of radiation. *J. Phys. C: Solid State Phys.* **15**,
398 3967-3985 (1982).
399 (39) T. Kirchartz, et al. Photoluminescence-based characterization of halide perovskites for
400 photovoltaics. *Adv. Energy Mater.* **14**, 1904134 (2020).
401 (40) D. Prochowicz, et al. Influence of A-site cations on the open-circuit voltage of efficient
402 perovskite solar cells: a case of rubidium and guanidinium additives. *J. Mater. Chen. A* **7**, 8218-
403 8225 (2019).
404 (41) F. Zhang, et al. Ultraviolet photoemission spectroscopy and Kelvin probe measurement
405 on metal halide perovskites: advantages and pitfalls, *Adv. Energy Mater.*, **10**, 1903252 (2020).
406 (42) L.A.A. Pettersson, et al. Modeling photocurrent action spectra of photovoltaic devices
407 based on organic thin films. *J. Appl. Phys.*, **86**, 487 (1999).
408 (43) M. Jeong, et al. Stable perovskite solar cells with efficiency exceeding 24.8% and 0.3-V
409 voltage loss. *Science* **369**, 1615-1620 (2020).
410 (44) P. Li, et al. Inkjet manipulated homogeneous large size perovskite grains for efficient and
411 large-area perovskite solar cells. *Nano Energy* **46**, 203-211 (2018).
412 (45) J.G. Tait, et al. Rapid composition screening for perovskite photovoltaics via concurrently
413 pumped ultrasonic spray coating. *J. Mater. Chem. A* **4**, 3792-3797 (2016).
414 (46) F.D. Giacomo, et al. Up-scalable sheet-to-sheet production of high efficiency perovskite
415 module and solar cells on 6-in. substrate using slot die coating. *Solar Energy Mater. and Solar*
416 *cells* **181**, 53-59 (2018).
417 (47) Y. Deng, et al. Surfactant-controlled ink drying enables high-speed deposition of
418 perovskite films for efficient photovoltaic modules. *Nat. Energy* **3**, 560-566 (2018).
419 (48) G. Fu, et al. Efficient enhancement in planar $CH_3NH_3PbI_{3-x}Cl_x$ perovskte solar cells by
420 processing with bidentate halogenated additives. *Solar Energy Mater. and Solar cells* **165**, 36-
421 44 (2017).
422 (49) E. Bi, et al. Efficient perovksite solar cell modules with high stability enabled by iodide
423 diffusion barriers. *Joule* **3**, 2748-2760 (2019).
424 (50) A. Priyadarshi, et al. A large area (70 cm^2) monilithic perovskite solar module with a high
425 efficiency and stability. *Energy Environ. Sci.* **9**, 3687-3692 (2016).

426
427 **Acknowledgements:**
428

the conclusions in the paper are present in the paper or the Supplementary Materials.

Supplementary Materials:
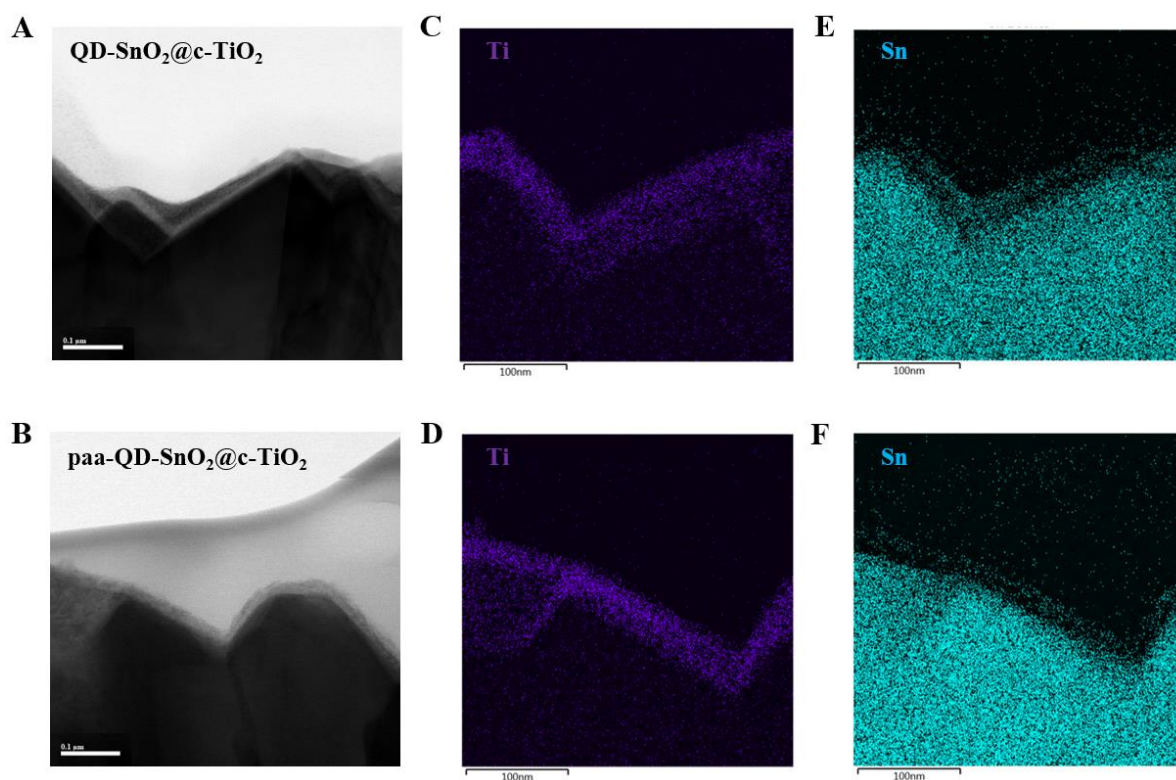
Figure 1. Microstructures of the ETLs. (**A** and **B**) The cross-sectional TEM images of the QD-SnO$_2$@c-TiO$_2$ (A) and paa-QD-SnO$_2$@c-TiO$_2$ over the FTO substrates. (**C** and **D**) EDS elemental analysis of Ti for both QD-SnO$_2$@c-TiO$_2$ (C) and paa-QD-SnO$_2$@c-TiO$_2$ (D) over the FTO surface. (**E** and **F**) EDS elemental analysis of Sn for both QD-SnO$_2$@c-TiO$_2$ (E) and paa-QD-SnO$_2$@c-TiO$_2$ (F) over the FTO surface.

10

480
481
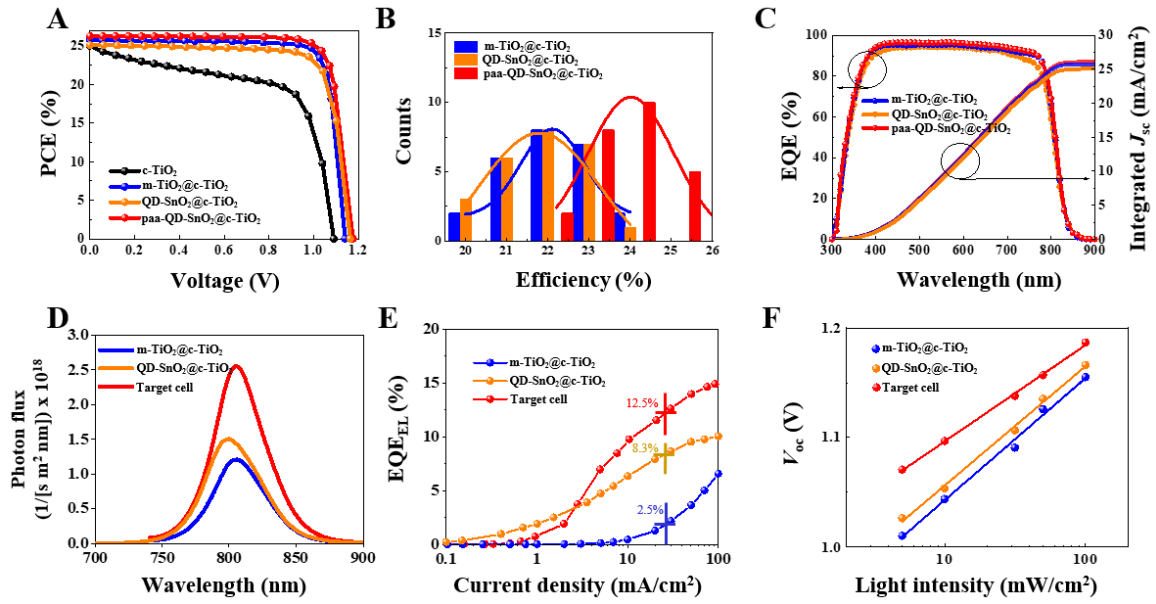
Figure 2. Characterization of the PSCs. (**A**) The *J-V* curves of the PSCs with different ETLs measured under the QSS-*IV* method. (**B**) A statistic distribution of the PCE for PSCs with different ETLs. (**C** to **F**) The EQE and integrated J_{sc} (C), Steady-state PL spectral photon flux (D), EQE$_{EL}$ (E) and the light dependent V_{oc} (F) for the PSCs with different ETLs.

486

11
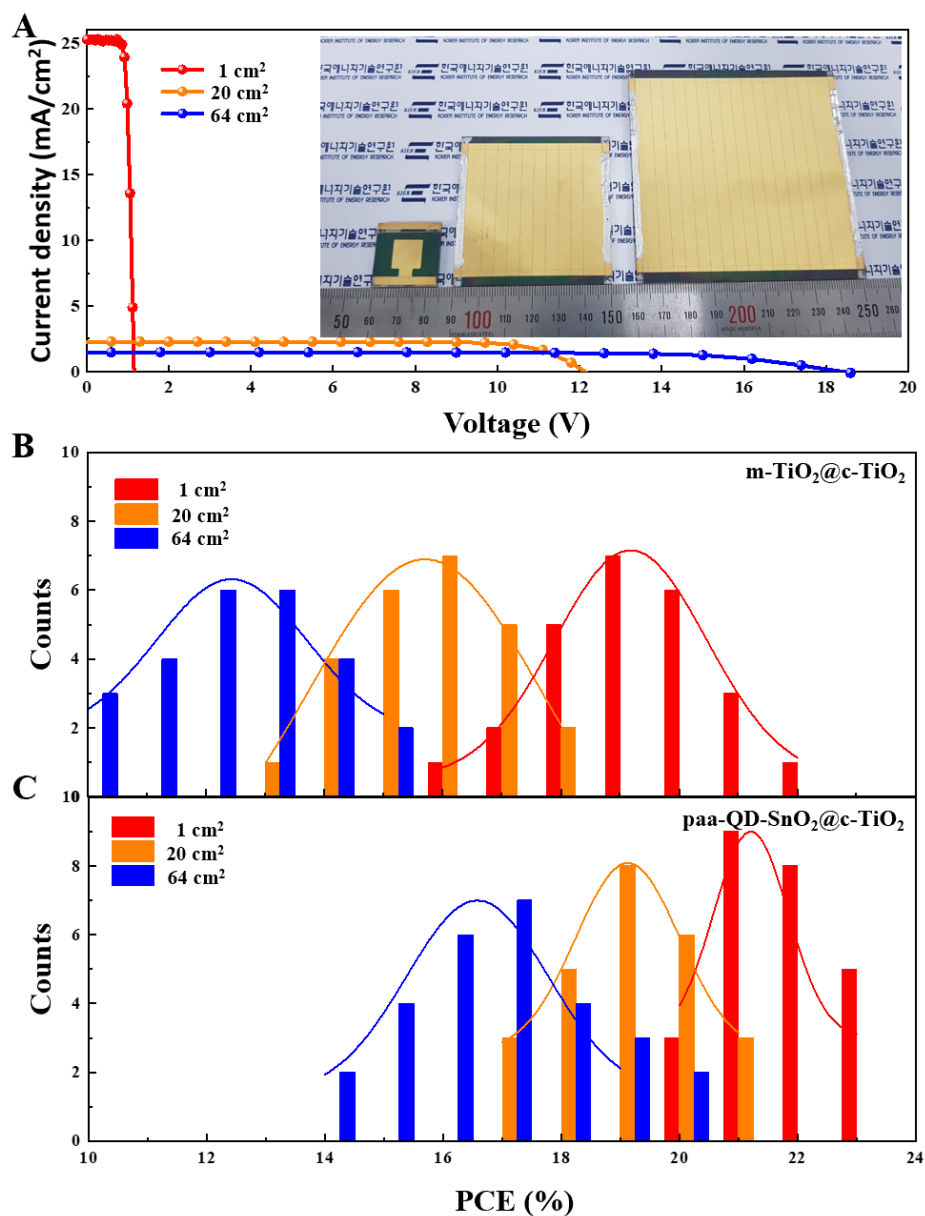
Figure 3. Performance of the large-size PSCs. (**A**) *J-V* curves of the large-size PSCs. The inserted picture is a photo images of the large-size PSCs. (**B** and **C**) Statistic distributions of the PCEs for the m-TiO$_2$@c-TiO$_2$ (B) and paa-QD-SnO$_2$@c-TiO$_2$ (C) based PSCs with pixel sizes of 1, 20 and 64 cm^2.

12
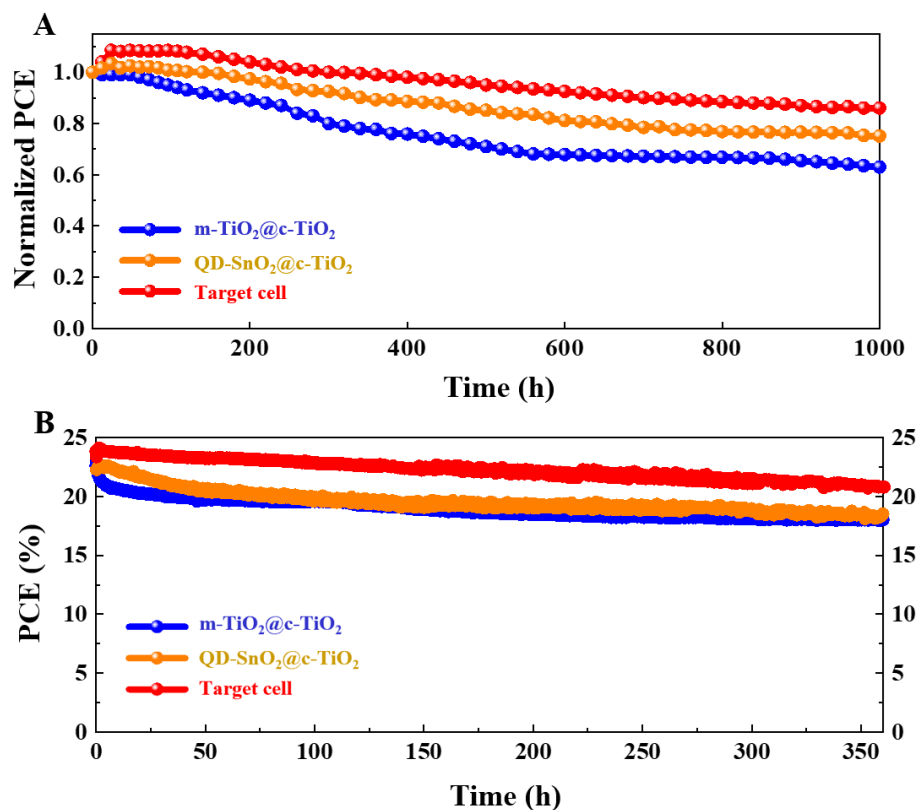
Figure 4. Stability of the PSCs with different ETLs. The stability shown here represents the best stability results of our four tested samples. (**A**) Shelf life of the unencapsulated PSCs tested in ambient air at 25% RH and 25 ℃ with different ETLs. (**B**) the operational stability test of the unencapsulated PSCs under MPP tracking conditions in a N_2 environment.